Tom E. W. Nicholas
Department of Mechanical Engineering,
University of Bath,
Claverton Down,
Bath, BA2 7AY, United Kingdom
email: tewn20@bath.ac.uk

James A. Scobie
Department of Mechanical Engineering,
University of Bath,
Claverton Down,
Bath, BA2 7AY, United Kingdom
email: j.a.scobie@bath.ac.uk

Gary D. Lock
Department of Mechanical Engineering,
University of Bath,
Claverton Down,
Bath, BA2 7AY, United Kingdom
email: ensgdl@bath.ac.uk

Hui Tang[1]
Department of Mechanical Engineering,
University of Bath,
Claverton Down,
Bath, BA2 7AY, United Kingdom
email: h.tang2@bath.ac.uk

A Model of Mass and Heat Transfer for Disc Temperature Prediction in Open Compressor Cavities

Accurate prediction of heat transfer in compressor cavities is crucial to the design of efficient and reliable aircraft engines. The heat transfer affects the thermal expansion of the compressor rotor and, in turn, the tip clearance of the compressor blades. This paper presents a novel, physically-based predictive theoretical model of heat transfer and flow structure in an open compressor cavity, which can be used to accurately calculate disc temperatures. The radially higher region of the cavity is dominated by buoyancy effects created by the temperature difference between the hot mainstream flow and the axial throughflow used to cool the turbine. Strong interaction between the air in the cavity and this throughflow creates a mixing region at low radius. For a given geometry, the heat transfer and flow physics are governed by four parameters: the rotational Reynolds number Re_ϕ, the buoyancy parameter $\beta\Delta T$, the compressibility parameter χ, and the Rossby number Ro. The model quantifies both the buoyancy- and throughflow-induced mass and heat transfer, producing a reliable prediction of the disc and air temperatures. The model takes into account a two-fold effect of the throughflow: being entrained into the cold radial plumes directly and creating a toroidal vortex in the radially lower region of the cavity. The exchange of mass between the cavity and throughflow is related to the mass flow rate in the radial plumes in the buoyancy-induced region, considering the effect of flow reversal at low Ro. The model is validated using data collected in the Bath Compressor Cavity Rig and can be incorporated in engine design codes to robustly compute the thermal stress and expansion of the compressor rotor, contributing to more efficient engine designs.

Keywords: buoyancy-induced flow, rotating cavity, theoretical modelling, high-pressure compressor

1 Introduction

The modelling of temperatures in gas turbine high-pressure compressors is vital for the design of the next-generation engines operating in the worsening climate crisis. Future engines will have pressure ratios above 70:1, which will lead to correspondingly shorter blades and in turn increased sensitivity to tip clearance. These tip clearances must be controlled accurately to maintain a high level of efficiency with new engine designs. The clearance between the blades and the outer casing is strongly affected by the thermal growth of the discs to which these blades are attached. The thermal growth is determined by the temperature distribution within the compressor rotor and it is essential to understand the governing conjugate heat transfer mechanisms and flow physics driving the gradients in metal temperatures. A typical compressor rotor is shown in Figure 1, highlighting a cavity formed by two co-rotating discs and the shroud at the disc periphery. Typical industrial designs include cobs at the bore, which introduce geometric factors that influence the fluid dynamics and heat transfer.

Owing to the high rotational speed and the temperature difference between the hot shroud and the cold axial throughflow, the flow in these cavities is buoyancy-induced, making it unsteady, unstable, asymmetric and three-dimensional. The heat transfer in these cavities is dominated by free convection, which is analogous to Rayleigh-Bénard convection between stationary horizontal plates but driven by centrifugal forces rather than gravity. This flow structure is disrupted and complicated by the exchange of heat and mass with the axial throughflow of cooling air, in so-called open cavities. The mechanisms that drive the interaction and the corresponding scaling laws are unclear. The complexity of the problem limits the use of numerical models to predict disc temperatures in the iterative engine design process. However, reduced-order modelling of the flow and heat transfer is a valuable and expedient tool for the designer.

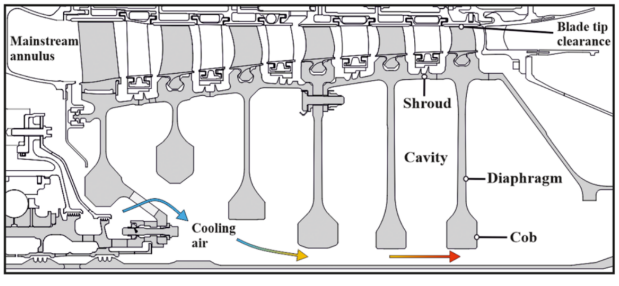

Fig. 1 Diagram of a compressor core, with a cross-section of an open cavity, from Jackson *et al.* [1].

This paper presents a new model for flow and heat transfer in rotating compressor cavities. The predictive model has been used to generate disc and core temperatures over a range of practical operating conditions. The model is validated by good agreement with disc temperature and shroud heat flux measurements from the Bath Compressor Cavity Rig across a range of parameter values. Section 2 provides a review of previous research, focusing on the

[1]Corresponding Author.
Version 1.18, November 10, 2023

interaction between the cavity flow and axial throughflow. Section 3 discusses the plume model for buoyancy-induced flow in a closed cavity and the calculation of shroud heat transfer and plume mass flow rate. Section 4 details the new model applied to open cavities, herein referred to as the open cavity model. Section 5 presents the results of the model compared to experimental disc temperatures and shroud heat fluxes. Section 6 summarises the main conclusions.

2 Review of Relevant Work

Owen and Long [2] reviewed a wide range of research on buoyancy-induced flow. Previous work often focused on the flow and heat transfer in the buoyancy-induced region. In some cases, the simplified geometry of a closed cavity was used, where the cobs are contiguous and the rotating flow structure in the cavity is isolated from external fluid dynamics. The following review is focused on the effect of axial throughflow on the flow and heat transfer in open rotating cavities.

Flow Structure

Owen and Pincombe [3] investigated the flow phenomenon in isothermal open cavities using flow visualisation and Laser-Doppler Anemometry (LDA). It was shown that the throughflow creates a toroidal vortex in the cavity and the distortion and radial extent of the vortex were dependent on the Rossby number, Ro, which is equivalent to the ratio between the axial Reynolds number Re_z and the rotating Reynolds number Re_ϕ. These parameters are defined as

$$\mathrm{Re}_z = \frac{\rho W d_H}{\mu} \tag{1}$$

$$\mathrm{Re}_\phi = \frac{\rho \Omega a}{\mu} \tag{2}$$

$$\mathrm{Ro} = \frac{W}{\Omega a} \tag{3}$$

where W is the average axial velocity of the throughflow, Ω the rotational speed of the disc, d_H the hydrodynamic diameter of the throughflow and a the inner radius of the cavity. Other symbols are defined in the nomenclature. The behaviour of vortex breakdown was observed to be dependent on Ro. At low Ro the resulting flow behaviour became sensitive to the temperature difference between the shroud and the throughflow, commonly denoted by the buoyancy parameter, $\beta\Delta T$:

$$\beta\Delta T = \frac{T_{sh} - T_1}{T_1}. \tag{4}$$

where T_{sh} is the cavity shroud temperature and T_1 is the axial throughflow temperature.

Farthing *et al.* [4] conducted one of the first notable studies into flow structure in heated open cavities. The flow visualisation suggested the existence of cyclonic and anti-cyclonic vortex pairs. The cold throughflow entered the cavity via radial plumes between these vortices, which were referred to as "radial arms". The LDA measurements showed the slip speed of the vortical structures first increased and then decreased with increasing Ro, and it increased monotonically as $\beta\Delta T$ increased. It was also stated that for almost all practical cases in gas turbine engines Ro < 1. Long *et al.* [5] used LDA measurements to find the axial, radial and tangential velocities in heated open cavities under engine-representative conditions. The data indicated the structure in the high-radius region of the cavity dominated by buoyancy-induced flow had a proportional dependency on Re_ϕ, but was insensitive to Re_z. Fazeli *et al.* [6] used LDA measurements to study the flow structure and compared the results with Unsteady Reynolds-Average Navier-Stokes (URANS) calculations. They showed the cavity was separated into two regions: one dominated by bore flow and the other by buoyancy. The CFD results showed Rayleigh-Bénard convection cells carrying cold fluid radially outward from the bore to the shroud and hot fluid inward from the shroud to the bore.

Experimental studies have also assessed the fraction of the axial throughflow entering the cavity. Black and Long [7] used Coherent Anti-Stokes Raman Spectroscopy to find the fraction was almost invariant with Ro ($40 - 47\%$ for $0.3 < \mathrm{Ro} < 1.5$) for a fixed Re_ϕ. Long [8] used a heat balance method to determine the fraction $\sim 10\%$ at Ro = 10. Günther *et al.* [9] used a similar heat balance method and showed that the fraction decreased as Ro increased.

Jackson *et al.* [10] investigated the flow structure in an open cavity using unsteady pressure measurements for $0.4 < \mathrm{Ro} < 1$. The strength of the vortices was shown to increase with $\beta\Delta T$, and the slip of the structures reached a maximum for Ro = 0.4. In further research from Jackson *et al.* [1], the authors noted that at Ro = 0.2 there is rotationally induced axial outflow in the upper region of the bore, referred to as *reversal flow*, which occurs for low Ro. Gao and Chew [11] conducted Wall-Modelled Large-Eddy Simulations (WMLES) of the flow and heat transfer in the cavity used by Jackson *et al.* [10]. The flow structures for Ro>0.4 were investigated, and it was shown that the cold axial throughflow was entrained into the cold plumes, and that hot fluid left the cavity via the hot plumes. The calculated axial velocity in the throughflow indicated flow reversal near the disc cobs, and the reversal flow decreased as Ro was increased. Moreover, consistent with the Large-Eddy Simulation (LES) calculations conducted by Pitz *et al.* [12] and Saini and Sandberg [13], laminar Ekman layers were presented on disc surfaces. The mass flow exchange between the bore and cavity flow was shown to increase as $\beta\Delta T$ increased and Ro decreased.

The current research has shown that the flow structure in the open cavity is strongly dependent on Ro. The effect of the throughflow is two-fold: generating a toroidal vortex in an inner region near the cobs and influencing the outer region at high radius dominated by Rayleigh-Bénard flow via radial plumes. The influence of Ro on the mass exchange in the cavity is of particular interest as this determines the core temperature and heat that is transferred from the cavity. Although no consistent effects of Ro were observed, in general the fraction of axial throughflow entering the cavity decreases as Ro increases. However, the driving mechanism and the corresponding scaling laws are still unclear. Moreover, experimental and computational studies have provided evidence for *reversal flow* in the axial throughflow path at low Ro. The theoretical model here aims to determine the exchange mass flow based on the plume mass flow in the cavity instead of the axial throughflow, taking into account the effects of reversal flow.

Temperature and Heat Transfer

Long and Childs [14] measured the shroud heat transfer in open cavities for a range of non-dimensional engine-representative conditions using surface temperatures and a conduction solution method. A correlation for Rayleigh-Bénard convection was developed for the shroud Nusselt number (Nu) and Grashof number (Gr). Buoyancy-induced flow was first theoretically modelled by Owen and Tang [15]. The laminar Ekman-layer equations were used to model the disc heat transfer. The model also predicted that at high Re_ϕ, the core temperature increases with radius due to the effects of compressibility, leading to reduced heat transfer on both discs and shroud. Linear equations for flow in the inviscid core, the equations for the compressibility effect, and a conduction model for the disc were also applied together with the laminar Ekman layer solution to predict the disc temperature and heat transfer. These were in good agreement with the temperature measurements in Atkins and Kanjirakkad [16] and Tang *et al.* [17].

Jackson *et al.* [18] conducted an experimental study into heat transfer in the open cavity. Disc heat fluxes were derived using the Bayesian approach developed by Tang *et al.* [19] and compared with predictions from the Owen-Tang model. The experiments

captured the attenuation of heat transfer caused by compressibility at high rotational speeds. Jackson *et al.* [1] conducted steady-state heat flux measurements to generate a correlation between the shroud Nu and Gr. The Rayleigh-Bénard type correlation was based on cavity air temperatures adjacent to the shroud, which were determined using the Owen-Tang buoyancy model. The simulated disc heat fluxes from Gao and Chew [11] showed good agreement with the experimental values from Jackson *et al.* [10]. The calculated air temperature revealed a significant temperature gradient within the laminar Ekman layer, showing that Ekman-layer conduction dominates disc heat transfer, especially at high radii and large Gr.

Research on heat transfer in open cavities has generated correlations between the shroud heat transfer and Gr, the laminar behaviour of the disc heat transfer, and the dependency of heat transfer on the throughflow Ro. However, there is no functional, quantifiable relationship between the effect of the throughflow and the heat transfer and mass exchange in open cavities. Although the previous Owen-Tang Model is capable of capturing the buoyancy effect, it did not incorporate the mass flow exchange between the cavity flow and the throughflow, or the effects of *reversal flow*. In this paper, a new predictive theoretical model is developed to predict this interaction and the disc and core temperatures in open cavities.

3 Plume model for the buoyancy-induced flow and heat transfer

Theoretical studies of buoyancy-induced flow and heat transfer have been conducted in simplified compressor cavities where there is no axial gap between the adjacent disc cobs. Here the closed cavity forms a rotating annulus and the flow structure is not influenced by the throughflow (Ro = 0). These studies act as fundamental investigations but do not simulate the open cavities found in most practical gas turbines. Before discussing the equations for the new model for open cavities, a brief description is given of the plume model proposed for closed cavities by Tang and Owen [20] and further developed by Nicholas *et al.* [21].

3.1 Plume Mass Flow Rate. The principal assumption of the model is that plumes of radially moving fluid act as the mechanism for convective heat transfer from the hot shroud to the low radius areas of the cavity. Pairs of anti-cyclonic and cyclonic vortices form and provide the necessary Coriolis forces for radial flow in the core. The plume mass flow rate can be non-dimensionalised using ψ, and can be linked to the circumferential pressure variation via

$$\psi_p = \frac{\dot{m}_p}{\mu s} = \frac{n \mathrm{Re}_\phi C_{\Delta p}}{2}. \tag{5}$$

Here, n is the number of vortex pairs and $C_{\Delta p}$ is the non-dimensional circumferential pressure variation, determined experimentally from the high-frequency pressure measurements in the cavity:

$$C_{\Delta p} = \frac{\Delta p}{\rho_c \Omega_c^2 b^2}, \tag{6}$$

where Δp is the pressure difference between the anti-cyclonic and cyclonic vortices in the cavity.

Lock *et al.* [22] correlated ψ_p with the shroud Grashof number,

$$\mathrm{Gr}_{sh} = \mathrm{Re}_\phi^2 \beta \Delta T_{sh} \left(\frac{s/2}{b}\right)^3 \tag{7}$$

where $\beta \Delta T_{sh}$ is defined based on the core temperature near the shroud,

$$\beta \Delta T_{sh} = \frac{T_{sh} - T_{c,b}}{T_{c,b}}. \tag{8}$$

Pernak *et al.* [23] corrected the correlation from [22] for the non-adiabatic boundary conditions, and generated a correlation for the open cavity of the Bath Compressor Cavity Rig, shown as follows:

$$\psi_p = 38.4 (\mathrm{Gr}_{sh} \mathrm{Pr})^{0.39}, \tag{9}$$

where Pr is the Prandtl number defined by the fluid properties.

The plume model assumed that the mass flow rate in the cold plumes was equal to that of the hot plumes. This assumption is only true if the radial flow in the Ekman layers is negligible compared to the radial plume flow rate. The Ekman layer mass flow, ψ_E, is given by

$$\psi_E = \pi \mathrm{Re}_\phi (r/b)^2 \left(\frac{\mu}{\rho \Omega}\right)^{1/2} (1 - \Omega_s/\Omega_d) \frac{b}{s}, \tag{10}$$

where Ω_s is the angular velocity of the structures [24]. Even at a slip of 15%, such that $\Omega_s/\Omega_d = 0.85$, ψ_E is still at least an order of magnitude less than that in the plumes.

3.2 Heat Transfer. Consistent with previous studies, the plume model assumes that the heat transfer at the shroud is governed by a free convection layer on the shroud surface. The heat transfer at the shroud is correlated to the temperature difference between the shroud and the core, and the rotational speed. This is analogous to Rayleigh-Bénard free convection correlations with gravitational acceleration replaced by centripetal acceleration. Lock *et al.* [22] developed a correlation for the closed cavity using heat flux measurements and the plume model. Nicholas *et al.* [21] extended the plume model to transient operating conditions and applied a similar correlation to the prediction of transient shroud heat fluxes. Pernak *et al.* [23] developed a new correlation for the open cavity using optimised core temperatures and measured shroud heat flux; this was found to be identical to the laminar flat-plate correlation, given by

$$\mathrm{Nu}_{sh} = 0.54 (\mathrm{Gr}_{sh} \mathrm{Pr})^{0.25} \tag{11}$$

where the shroud Nusselt number is defined as follows:

$$\mathrm{Nu}_{sh} = \frac{q_{sh} s/2}{k \Delta T_{sh}}. \tag{12}$$

The plume model assumes the temperature in the core is the mean of the hot and cold plume temperatures, such that the circumferentially-averaged core temperature is given by

$$T_c = \frac{T_{\check{p}} + T_{\hat{p}}}{2}, \tag{13}$$

where $T_{\check{p}}$ and$T_{\hat{p}}$ are the hot and cold plume temperatures, respectively. These temperatures vary with radius. The radial distribution of core temperature is driven by compressibility and heat transfer to and from the disc. Section 4.3 provides further detail, and the full derivations are given by Tang and Owen [20], where laminar conductive Ekman layers are assumed, with a match to experimentally measured disc temperatures.

4 Model of heat transfer in open cavities

The closed cavity plume model correlated the plume mass flow rate with shroud heat transfer and, in turn, the Grashof number. The new model links this plume mass flow to the exchange mass flow rate with the axial throughflow, establishing the inter-dependency between the flow structure and heat transfer in heated open cavities. As shown in Figure 2, the model divides the cavity into two distinct sections: the inner region, where the flow structure is driven mainly by the interaction with the throughflow and associated toroidal vortex; and the outer region, where the flow structure is driven by buoyancy forces. Here, it is assumed that the boundary

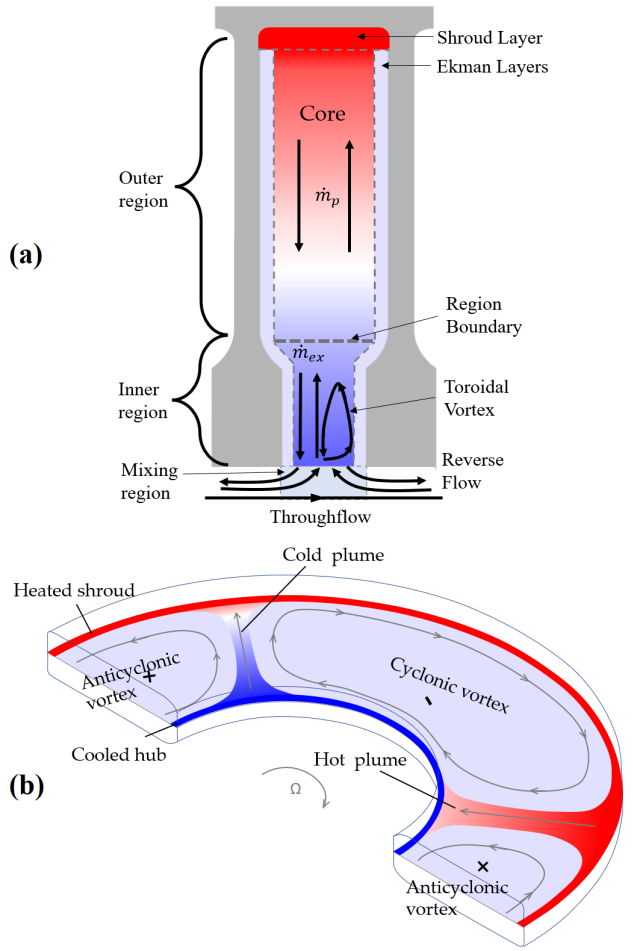

Fig. 2 Flow structure in the open cavity with two pairs of rotating structures. (a) a cross-section of the circumferentially averaged temperature contours, and (b) shows the midplane temperature contours and flow direction in the outer region of the cavity.

between the two regions is the start of the diaphragm section. The toroidal vortex is enhanced as Ro is increased. As discussed above, flow reversal can occur in the axial throughflow at low Ro, increasing throughflow and core temperatures. This section explains the physical principles and the mathematical equations for the model.

4.1 Exchange of mass and heat transfer between cavity flow and axial throughflow. Figure 2 shows a diagram of a typical open cavity, which is formed by two co-rotating discs and the rotor shroud. The boundary between the inner and outer regions is assumed to be the start of the disc diaphragm. It is assumed there is a control volume in the axial throughflow path in which cold air can be entrained into the cavity and hot air can be entrained into the throughflow. This is shown in Figure 3. The average temperature of the axial throughflow entering and exiting the control volume are T_1 and T_2, respectively. Cold fluid is entrained at $\dot{m}_{ex}$ into the cavity from the control volume with an average temperature of $T_{\check{p},a}$ and an equal amount of hot fluid enters the control volume from the cavity with an average temperature of $T_{\hat{p},a}$. The subscript a is used to indicate temperatures at the lower radius of the cavity.

As discussed above, at low Ro there is flow reversal within the axial throughflow, influencing the temperature of the fluid entrained into the cavity. The reversal flow has a mass flow rate $\dot{m}_r$, and decreases to zero above a critical Ro. The reversal flows leave the mixing region with a temperature of $T_{\check{p},a}$ at both the upstream and

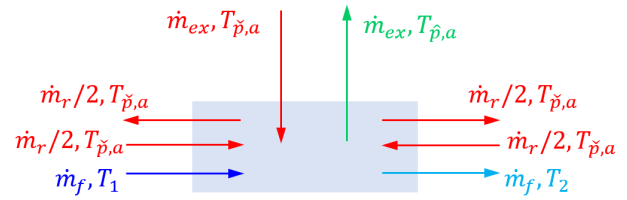

Fig. 3 Mixing control volume between throughflow and cavity air.

downstream sides and re-enter the region with the same temperature (it is assumed that the enthalpy exchange between the reversal flow and throughflow is negligible). When there is no reversal flow, the entrained flow or the exchange flow is assumed to leave the mixing region with the temperature of the throughflow, T_1, i.e. $T_{\hat{p},a} = T_1$. When there are reversal flows, the exchange flow temperature is increased owing to the exchange of enthalpy with the hot plume temperature, $T_{\check{p},a}$. It follows that

$$T_{\hat{p},a} = \frac{(\dot{m}_{ex} - \dot{m}_r)T_1 + \dot{m}_r T_{\check{p},a}}{\dot{m}_{ex}} \tag{14}$$

where $\dot{m}_{ex}$ and $\dot{m}_r$ are the mass flow rates of the exchange and reversal flows.

From the conservation of energy,

$$\dot{m}_f(T_2 - T_1) = \dot{m}_{ex}(T_{\check{p},a} - T_{\hat{p},a}), \tag{15}$$

where $\dot{m}_f$ is the axial throughflow mass flow rate. Note that the change of kinetic energy is ignored at this stage.

The reversal mass flow rate approaches that of the entrained flow at low Ro values and reduces to zero at high Ro values. It is assumed that the reversal flow follows a negative linear trend, and is equal to zero above a critical Ro. The reversal flow is also affected by the buoyancy parameter at the shroud, $\beta\Delta T_{sh}$. An increase in $\beta\Delta T_{sh}$ leads to a larger increase in the plume mass flow than the reversal flow rate, reducing the relative effect of flow recirculation. This effect is less significant than that of Ro and it is accounted for using a scaling exponent of 0.25. In non-dimensional form,

$$\frac{\psi_r}{\psi_{ex}} = \begin{cases} 1 - \frac{\mathrm{Ro}\beta\Delta T_{sh}^{0.25}}{A_1}, & \mathrm{Ro}\beta\Delta T_{sh}^{0.25} \le A_1 \\ 0, & \mathrm{Ro}\beta\Delta T_{sh}^{0.25} > A_1 \end{cases} \tag{16}$$

where A_1 is an empirical value. The value of this parameter was found by achieving the best agreement between predicted and measured disc temperatures. This gave $A_1 = 0.244$. As a result, there is no reversal flow for approximately Ro > 0.4 for the given range of $\beta\Delta T_{sh}$. This value is also consistent with the Ro value in Jackson *et al.* [18] where the pressure variation and slip speed were at their maxima.

4.2 Cavity flow structure and plume temperatures. As stated, the flow in the core is divided into the inner and outer separated by the cob geometry, as shown in Figure 2. In the outer region, with a cavity width of s, the mass flow in the radial plumes ψ_p transfer heat from the shroud and discs to the inner region. In the inner region, with reduced cavity width s' (due to the thickness of the cobs, see Figure 2 for the axial width of the radially lower region) the mass flow rate of the plumes is reduced to the exchange mass flow rate, ψ_{ex}. The cold entrained flow from the axial throughflow combines with the recirculated flow from the outer region to make the cold radial plume in the outer region. A part of the hot radial plume in the outer region flows radially inward into the axial throughflow. The conservation of mass is satisfied as the radial inflows and outflows are equal at every radial location. For a perfect open cavity (i.e. with cob thickness equal

to that of the discs), and at low Ro, $\psi_{ex} = \psi_p$. For the closed cavity, $\psi_{ex} = 0$.

The exchange (or entrained) mass flow rate ψ_{ex} can be treated as a fraction of the outer region plume mass flow rate ψ_p, where this fraction is a function of the width ratio $\eta = s'/s$. For low Ro, this fraction is equal to η, which reduces as the cob separation reduces. As Ro increases, ψ_{ex} decreases as a result of the increased momentum in the toroidal vortex. The results also show that ψ_{ex} is affected by $\beta\Delta T_{sh}$. An increase in $\beta\Delta T_{sh}$ enhances the buoyancy-induced convection and suppresses the toroidal vortex. Therefore, ψ_{ex} is correlated to $Ro/\beta\Delta T_{sh}{}^{0.5}$ to account for both of these effects. Thus, the ratio of the flow rates is given by

$$\frac{\psi_{ex}}{\psi_p} = \frac{\eta}{1 + A_2(\frac{\mathrm{Ro}}{\beta\Delta T_{sh}{}^{0.5}})^l}, \tag{17}$$

where A_2 and l are empirical parameters, and $\beta\Delta T_{sh}$ is defined by Equation 8. For the open configuration in the Bath Compressor Cavity Rig used to validate the model, $\eta = 0.65$. These values are optimised, together with Equation 16, to produce the best agreement between theoretical and measured disc temperatures, giving $A_2 = 0.0.0217$ and $l = 3.21$. The resultant correlation, plotted against Ro, is shown in Figure 4.

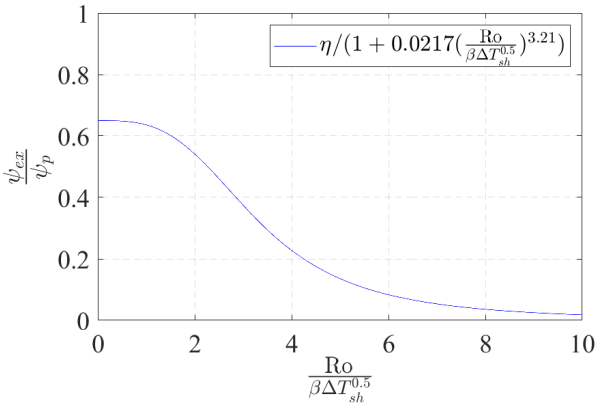

Fig. 4 Correlation for exchange mass flow as a fraction of the plume mass flow rate.

As discussed in Section 3.1, the plume mass flow is governed by the shroud Grashof number, and in the outer region, this can be determined using Equation 9.

Consider the interface between the two regions inside the cavity. The hot plumes in the outer region are the source of the hot plumes in the inner region, hence the hot plume temperatures for both regions at this interface are equal. However, the cold plume temperature exiting the inner region has mixed with the hot fluid from the outer region, increasing the cold plume temperature leaving the inner region. Consequently, there is a step change in the cold plume temperature at the interface and the temperature difference between the cold and hot plumes in the inner region is larger than that in the outer region.

Using the cavity as a control volume and from the conservation of energy, it follows that the temperature difference between the cold and hot plumes at any radius in the outer region is given by

$$c_p\dot{m}_p(T_{\check{p},r} - T_{\hat{p},r}) = \dot{Q}_{sh} + 4\pi\int_r^b h_d(T_d - T_c)r\,dr, \tag{18}$$

where $\dot{Q}_{sh}$ is the heat flow from the shroud to the core, T_d is the disc temperature, T_c is the core temperature, and h_d the disc heat transfer coefficient. In the open cavity, there are small temperature differences between the upstream and downstream discs, which gives different disc heat transfer values. Here, for simplicity, the averaged disc temperature is used to evaluate the average disc heat flux and then the flux is doubled to estimate heat transfer from both discs. The calculation of the disc temperature and the circumferentially-averaged core temperature, T_d and T_c, is given in Section 4.3.

Similarly, for the inner region, the enthalpy change of the exchange flow to the cavity can be calculated using

$$c_p\dot{m}_{ex}(T_{\check{p},a} - T_{\hat{p},a}) = \dot{Q}_{sh} + \dot{Q}_d. \tag{19}$$

As $T_{\hat{p},a}$ is the temperature of the flow that is entrained from the cool throughflow. To determine the shroud and disc heat transfer, the temperature changes $(T_{\check{p},a} - T_{\hat{p},a})$ and $(T_{\check{p},r} - T_{\hat{p},r})$ are calculated, which further determines the radial distributions of the plume temperature. The heat flow from the shroud, $\dot{Q}_{sh}$, and discs, $\dot{Q}_d$, is given by the following:

$$\dot{Q}_{sh} = 2\pi h_{sh}(T_{sh} - T_{c,b})bs, \tag{20}$$

$$\dot{Q}_d = 4\pi\int_a^b h_d(T_d - T_c)r(\cos\alpha)^{-1}dr, \tag{21}$$

where α is the angle (as a function of radius) between the elemental disc surface area and the radial direction, which is zero except for the fillet region where there is curvature of the disc surface.

The convective shroud and conductive laminar Ekman layer theories in Section 3 yield heat transfer coefficients on the shroud and discs:

$$h_{sh} = \frac{k\mathrm{Nu}_{sh}}{s/2} = \frac{k(C\mathrm{Gr}_{sh}^n)}{s/2}, \tag{22}$$

where $C = 0.54$ and $n = 0.25$ from Equation 11,

$$h_d = \frac{k\mathrm{Nu}_d}{b} = k/\sqrt{\frac{\mu}{\rho\Omega_d}}. \tag{23}$$

Equation 19 can be rewritten in a non-dimensional form as

$$\psi_{ex}(\theta_{\check{p}} - \theta_{\hat{p}}) = \frac{1}{\mathrm{Pr}G}[4\pi\mathrm{Nu}_{sh}(1 - \theta_{c,b}) +$$

$$2\pi\int_{x_a}^{x_b} x\mathrm{Nu}_d(\theta_d - \theta_c)(\cos\alpha)^{-1}dx], \tag{24}$$

where G is the cavity aspect ratio, s/b, and non-dimensional radius

$$x = \frac{r}{b} \tag{25}$$

and the non-dimensional temperature θ is defined relative to the axial throughflow as

$$\theta = \frac{T - T_1}{T_{sh} - T_1}. \tag{26}$$

4.3 Core and disc temperatures. From Equation 13, the non-dimensional core temperature is given by

$$\theta_c = \frac{\theta_{\hat{p}} + \theta_{\check{p}}}{2}. \tag{27}$$

Heat transfer from the disc to the core and the compressibility effect both lead to a radial increase in the plume temperatures. From this, and the plume mass flow rate in the outer region, the radial distribution of the core temperature in the outer region can be calculated using

$$\frac{d\theta_c}{dx} = 4\pi^2 x\frac{\mathrm{Nu}_d\mathrm{Nu}_{sh}}{\psi_p^2}\left[(1 - \theta_{c,b}) + \int_x^1 \frac{\mathrm{Nu}_d}{\mathrm{Nu}_{sh}}(\theta_d - \theta_c)x\,dx\right]$$

$$+(\gamma-1)x\chi. \tag{28}$$

where χ is the compressibility parameter,

$$\chi = \frac{\Omega_d^2 b^2/(\gamma R T_1)}{(T_{sh}-T_1)/T_1} = \frac{\mathrm{Ma}^2}{(T_{sh}-T_1)/T_1}. \tag{29}$$

Detailed derivation can be found in Tang and Owen [20].

Similarly, the core temperature in the inner region is determined using the exchange mass flow rate,

$$\frac{d\theta_c}{dx} = 4\pi^2 x \frac{\mathrm{Nu}_d \mathrm{Nu}_{sh}}{\psi_{ex}^2}[(1-\theta_{c,b})+$$

$$\int_x^1 \frac{\mathrm{Nu}_d}{\mathrm{Nu}_{sh}}(\theta_d-\theta_c)(\cos\alpha)^{-1}x dx] + (\gamma-1)x\chi. \tag{30}$$

Following the method of Nicholas *et al.* [21], the conjugate disc temperatures are calculated iteratively and using a 2-D Finite Element Analysis (FEA) solver and the steady-state 2-D heat equation,

$$\frac{\partial^2 T_d}{\partial r^2} + \frac{1}{r}\frac{\partial T_d}{\partial r} + \frac{\partial^2 T_d}{\partial z^2} = 0, \tag{31}$$

where z is the axial distance. The meshed geometry and the dimensions of the cavity are given in Figure 5. Note that a mesh grid sensitivity study was performed, showing that an order of magnitude finer mesh produced only a ~ 0.003 difference in calculated θ_d.

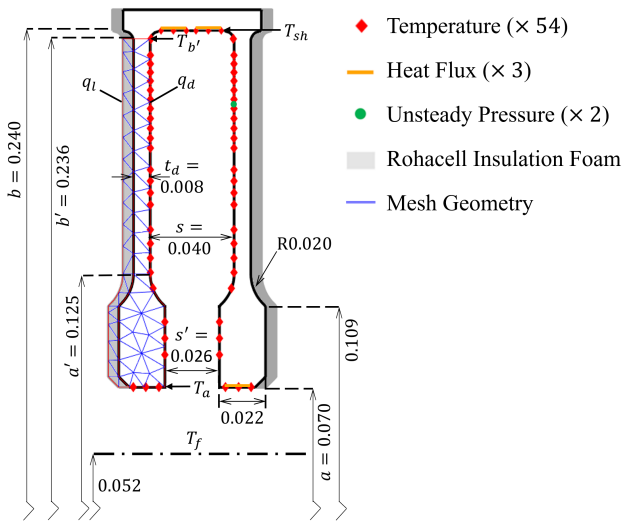

Fig. 5 Cross-section of the open cavity showing thermocouple locations, Rohacell foam, mesh geometry, and temperature and heat flux boundary conditions.

Figure 5 shows the test section of the Bath Compressor Cavity Rig, which features a 5 mm layer of low-conductivity Rohacell insulation foam. The back surfaces of the discs were not adiabatic and a non-negligible amount of heat is lost through the disc thickness. Note the back surfaces of the discs were adjacent to closed cavities upstream and downstream of the test section. Boundary conditions were required to solve the disc temperatures; Dirichlet boundary conditions were applied at the shroud and lower radius of the cob, taken from experimental measurements; and convective heat flux boundaries were applied on the disc and Rohacell surfaces. The shroud temperature was taken at the outer radius of the disc diaphragm due to the large change in temperature that occurs through the fillet at the shroud. The boundary conditions are used to solve Equation 31, written as

$$\begin{aligned}
T &= T_{d,b'}, \quad \text{at } r = b', \\
T &= T_{d,a}, \quad \text{at } r = a, \\
-k_d\frac{\partial T}{\partial z} &= q_d(t,r), \quad \text{on the front disc surface}, \\
k_d\frac{\partial T}{\partial z} &= q_l(t,r), \quad \text{on the back disc surface}, \\
T &= T_{d,0}(t,r,z), \quad \text{at } t = 0.
\end{aligned} \tag{32}$$

where the subscript l refers to the surface of the Rohacell, and

$$q_d = h_d(T_d - T_c), \tag{33}$$

$$q_l = h_d(T_d - T_l). \tag{34}$$

T_l is the air temperature in the cavity adjacent to the Rohacell surface, which is lower than that of the central cavity and higher than the throughflow, and so is assumed to follow $T_l = T_1 + (T_{sh} - T_1)/4$. However, the disc temperature was found to not be a strong function of T_l, where a 10% change in θ_l produced $< 1\%$ change in θ_d.

Equation 31 can be non-dimensionalised using the definition for θ in Equation 26,

$$\frac{\partial^2\theta_d}{\partial x^2} + \frac{1}{x}\frac{\partial\theta_d}{\partial x} + \frac{\partial^2\theta_d}{\partial y^2} = 0, \tag{35}$$

where the non-dimensional axial distance is

$$y = \frac{z}{b}. \tag{36}$$

The solver incorporates a non-dimensional heat flux term, defined by

$$\tau = \frac{2b^2 q}{k_d t_d (T_{sh} - T_1)}. \tag{37}$$

4.4 Solution technique. Figure 6 shows a flowchart of the solution technique to solve the open cavity model. The MATLAB PDE solver was used to solve Equation 35. As discussed above, this required Dirichlet conditions, $\theta_{d,a}$ and $\theta_{d,b'}$, and convective boundary conditions using the core temperatures in the central cavity, θ_c, and adjacent to the Rohacell surface, θ_l.

A central difference scheme was used to solve the core temperature at each iteration, from Equations 28 and 30, where the core temperature at the interface between the upper and lower cavity regions, $\theta_{c,a'}$, was iterated until a solution was converged. This convergence is governed by Equation 14, which can be non-dimensionalised using

$$\theta_{\hat{p},a} = \frac{\psi_r}{\psi_{ex}}\theta_{\check{p},a}. \tag{38}$$

From the definition of θ in Equation 26, when there is no reversal flow the cold plume temperature is equal to the inlet throughflow temperature, $T_{\hat{p}} = T_1$, or $\theta_{\hat{p}} = 0$ (from Equation 26) .

$\theta_{\hat{p},a}$ is found from Equations 13 and 30; this is compared to the right-hand-side of Equation 38 and $\theta_{c,a'}$ is altered until these are equal within 0.001. Unlike the closed cavity, the calculation of the heat transfer is a four-parameter problem and so the model requires the following parameters as inputs: Re_ϕ, $\beta\Delta T$, χ and Ro. The calculation of the plume mass flow rate and shroud heat transfer requires empirical correlations, which are detailed in Sections 3.1

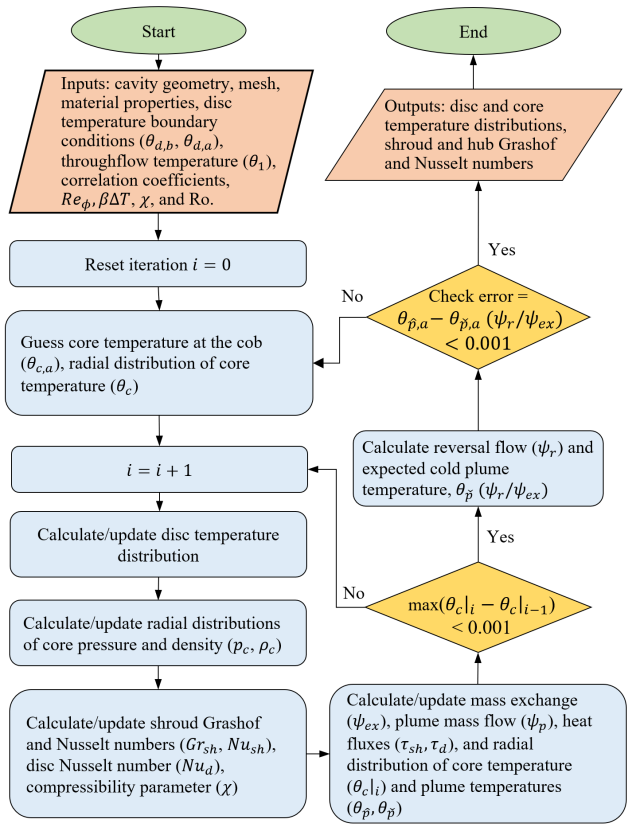

Fig. 6 Flowchart of the solution technique to the open cavity model.

and 3.2. Then the shroud heat flow is given by Equations 20 and 22, disc heat flow by Equation 21, ψ_p by Equation 9, ψ_{ex} by Equation 17, and ψ_r by Equation 16. The final output of the model is the resultant disc, core and plume temperature distributions, as well as shroud and disc Nusselt numbers.

5 Prediction of temperature and heat transfer in the open cavity of the Bath compressor cavity rig

5.1 Experimental Apparatus. The model is validated using steady-state results from the Bath Compressor Cavity Rig in the open cavity configuration. The rig simulates the conditions of both closed or open cavities in axial high-pressure compressors at engine-representative conditions. The design, operational parameters, and further specifics on the rig are described by Luberti *et al.* [25], and further detail on the open cavity cases presented here is given by Jackson *et al.* [18]. The test section features three cavities with data collected in the central cavity test section. The upstream and downstream closed cavities are isolated from the axial throughflow by Rohacell inserts.

Disc and shroud temperatures were measured using embedded thermocouples and their radial distributions are presented in Figure 5. The shroud heat flux was measured using a heat flux gauge, also shown in Figure 5. Temperature data on both the upstream and downstream disc surfaces have been used; the radial distributions on these discs were similar, so averaged values at the same radii are presented.

The non-dimensional parameters for the cases presented in this paper are given in Table 1. The detailed experimental data can be found in [18]. The flow Grashof number is defined using the throughflow temperature,

$$\mathrm{Gr} = \mathrm{Re}_\phi^2 \beta\Delta T. \tag{39}$$

Measured non-dimensional shroud heat flux values, τ_{sh} (Equation 37), from [10] are also listed in Table 1.

Table 1 Summary of parameters for the cases presented in this paper.

Case ID	N (RPM)	$Re_\phi/10^6$	$\beta\Delta T$	Ro	$\mathrm{Gr}/10^{11}$	χ	τ_{sh}
A_1	800	0.32	0.26	0.5	0.27	0.011	45
A_2	800	0.32	0.27	1	0.28	0.011	38
B_1	2000	0.8	0.27	0.2	1.7	0.066	59
B_2	2000	0.8	0.26	0.4	1.7	0.070	83
B_3	2000	0.8	0.25	0.8	1.6	0.073	75
B_4	2000	0.8	0.11	0.8	0.73	0.184	40
C_1	4000	1.6	0.1	0.4	2.5	0.83	78
C_2	4000	1.6	0.18	0.4	4.5	0.43	105
C_3	4000	1.6	0.26	0.4	6.5	0.28	121
D_1	6000	2.3	0.27	0.1	15	0.59	72
D_2	6000	2.3	0.26	0.2	14	0.63	106
D_3	6000	2.3	0.24	0.4	12	0.67	135
E	8000	3.0	0.24	0.2	22	1.2	106

5.2 Effect of $\beta\Delta T$ and Re_ϕ. Figure 7 shows the predicted radial distribution of non-dimensional disc and core temperatures. These are compared with experimental measurements of disc surface temperature, averaged across both upstream and downstream discs. There is remarkable agreement between the measured and predicted disc temperatures for all cases.

For Figure 7a, Ro and Re_ϕ are fixed at 0.4 and 1.6×10^6, respectively, and $\beta\Delta T$ is varied. It can be seen that the disc temperature is higher than the core temperature throughout most of the cavity leading to positive disc heat flux throughout. The figure also demonstrates the change in core temperature caused by the transition from the inner to the outer region of the cavity. In the outer region of the cavity, the plume temperature difference is driven by the plume mass flow rate calculated using the correlation in Equation 9, but in the inner region, this is driven by the exchange mass flow rate that is lower than ψ_p. This lower mass flow rate indicates a larger temperature difference between the plumes, and as the hot plume temperature in the inner region is assumed to be equal to the temperature in the outer region of the cavity at the interface, this alters both cold plume and core temperatures.

As shown by Figure 7a, for low Ro the non-dimensional disc temperatures are relatively insensitive to changes in $\beta\Delta T$. This is a result of high exchange flow, which means the cavity air temperature is subject to further flow recirculation in the mixing region. As $\beta\Delta T$ reduces, there is a slight increase in $\theta_{c,a}$ due to an increase in the reversal flow rate ψ_r. In addition, there is an increase in the gradient of non-dimensional core temperature θ_c as a result of the compressibility effect (which is relatively minor at $\mathrm{Re}_\phi = 1.6\times10^6$) making up a larger proportion of the temperature rise in the cavity as the shroud is cooler.

However, at higher Ro both the core and disc temperatures are more sensitive to $\beta\Delta T$. As shown in Figure 7b where Ro = 0.8, as $\beta\Delta T$ reduces, both the core and disc temperatures increase significantly. Under this condition, there is no reversal flow and the exchange mass flow is highly affected by the toroidal vortex. Therefore, a decrease in $\beta\Delta T$ enhances the toroidal vortex and decreases the exchange flow ratio (from Figure 4), increasing both the core and disc temperatures. This also causes a much larger step in core temperature, as the plume mass flow is far higher than the exchange mass flow.

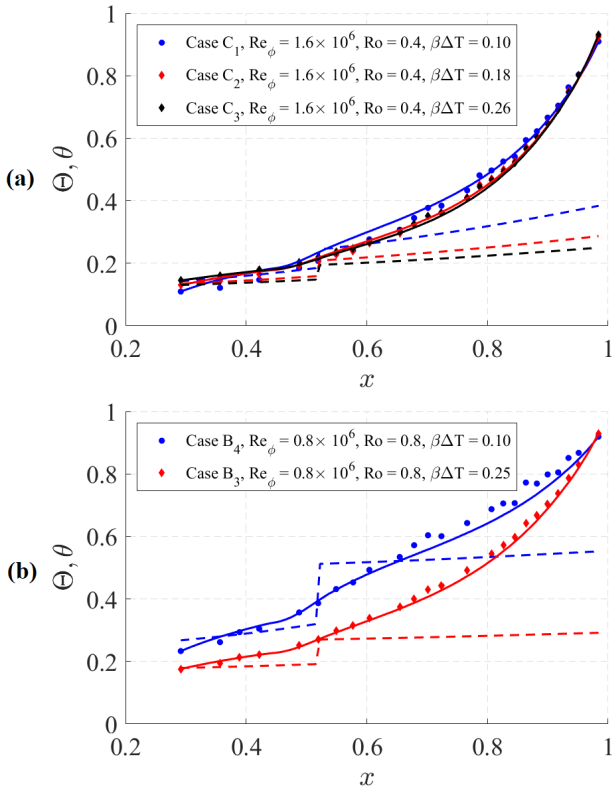

Fig. 7 Effect of $\beta\Delta T$ on the disc and core temperatures against non-dimensional radius at fixed Re_ϕ and fixed low Ro (a) and high Ro (b). Symbols represent experimental measurements. Solid lines denote the predicted disc temperatures and dashed lines the predicted core temperatures.

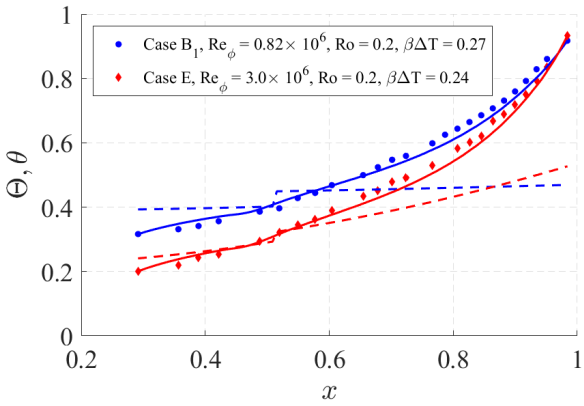

Fig. 8 Effect of Re_ϕ on the disc and core temperatures at fixed $\beta\Delta T$ and Ro. Symbols represent experimental measurements. Solid lines denote the predicted disc temperatures and dashed lines the predicted core temperatures.

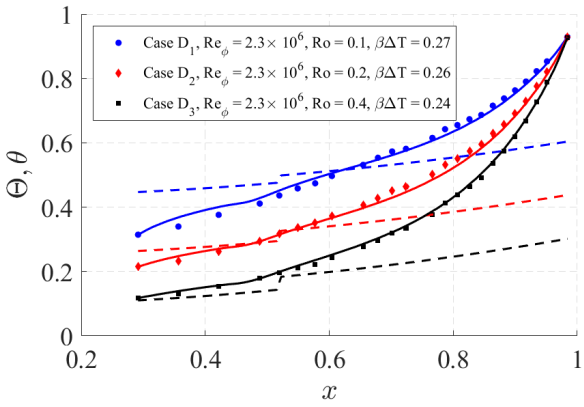

Fig. 9 Effect of Ro on the disc and core temperatures at $\beta\Delta T \approx 0.25$ and $Re_\phi = 2.3 \times 10^6$. Symbols represent experimental measurements. Solid lines denote the predicted disc temperatures and dashed lines the predicted core temperatures. Blue, red and black lines refer to increasing Ro, respectively.

Figure 8 shows the effect of rotational speed at a constant Ro of 0.4 and high $\beta\Delta T$. For these cases, θ_d is slightly underpredicted at higher radii, but the agreement is generally good. In the closed cavity, as shown by Tang and Owen [20] and Lock *et al.* [22], the distribution of θ_d was insensitive to Re_ϕ. However, in the open cavity where there is an exchange of mass between the cavity and the throughflow and angular momentum is not conserved, an increase in Re_ϕ significantly reduces θ_d at lower radii. This is the result of the axial Reynolds number Re_z increasing with Re_ϕ at constant Ro. The large radial increase in θ_c at high Re_ϕ is also shown here. As discussed in Lock *et al.* [22], as the compressibility parameter χ increases and θ_c approaches θ_d, the cavity approaches a flow structure similar to that expected during thermal stratification and weakened shroud heat transfer.

5.3 Effect of Ro. The impact of Ro on the distribution of θ_d and θ_c is more complex than the other governing parameters. As discussed in Section 4, increasing Ro reduces the reversal flow which increases the cold plume temperature. It also reduces the ratio of exchange mass flow to the plume mass flow rate, due to an enhanced toroidal vortex. Consequently, heat transfer between the cavity and throughflow air reaches a maximum at Ro $\sim$ 0.4, where the reversal flow is near zero and the exchange mass flow rate is still approximately equal to the width ratio, η.

Figure 9 shows the effect of increasing Ro from 0.1 to 0.4. It can be seen that although the exchange mass flow rate is approximately constant, increasing Ro reduces the core temperature due to the suppression of the reversal flow. Meanwhile, the shroud heat fluxes are increased, as shown in Table 1. Figure 10 shows the effect at Ro > 0.4. As Ro increases the core temperature increases due to the reduced ratio of exchange mass flow to the plume mass flow rate. This also increases the core temperature change from the inner to the outer region. The increased core temperature is also consistent with the decreased shroud heat transfer.

Figure 11 shows the cases with Ro less, equal and larger than 0.4. It is apparent that both the disc and core temperatures reach a minimum at Ro = 0.4, suggesting maximum heat transfer between the cavity and the throughflow. The measured values in Table 1 also agree with this trend. This trend was also observed in the core slip measurements conducted by Jackson et al.[18] where the slip speed reached a maximum at Ro $\approx$ 0.4. Similar trends were observed in Farthing *et al.* [4] where the core swirl in an open cavity (with no cobs or inner shaft) first decreased and then increased with increasing Ro. The turning point was observed at Ro $\approx$ 2.0, rather than 0.4. Although the qualitative relationship will be the same, the quantitative effects of reversal flow and the toroidal vortex are likely

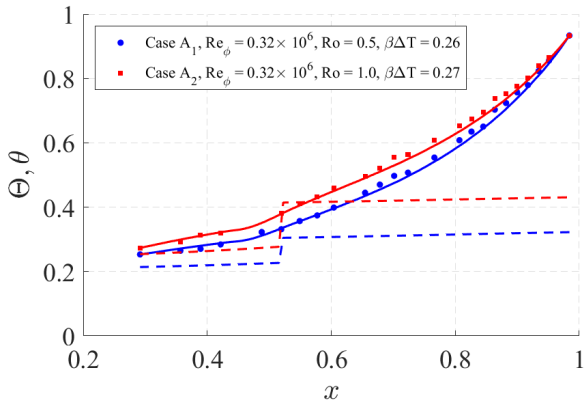

Fig. 10 Effect of Ro on the disc and core temperatures at $\beta\Delta T \approx 0.25$ and $Re_\phi = 3.2 \times 10^5$. Symbols represent experimental measurements. Solid lines denote the predicted disc temperatures and dashed lines the predicted core temperatures. Blue, red and black lines refer to increasing Ro, respectively.

to vary with the cavity geometry, the inlet swirl of the throughflow and the interaction with adjacent cavities. More experiments with different cavity configurations will contribute to the development of these relationships.

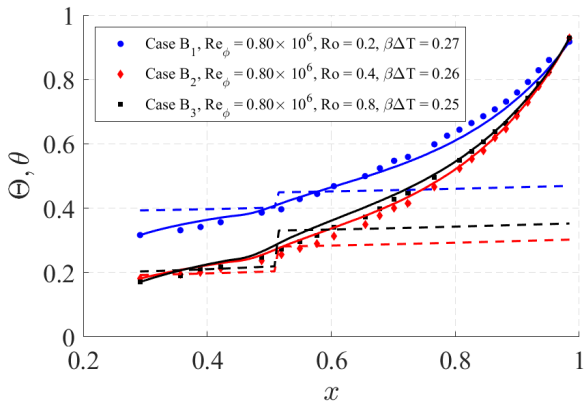

Fig. 11 Effect of Ro on the disc and core temperatures at $\beta\Delta T \approx 0.25$ and $Re_\phi = 8 \times 10^5$. Symbols represent experimental measurements. Solid lines denote the predicted disc temperatures and dashed lines the predicted core temperatures. Blue, red and black lines refer to increasing Ro, respectively.

6 Conclusions

A new model, referred to as the open cavity model, was developed to determine the flow and heat transfer in open compressor cavities, predicting the radial distribution of disc and core temperatures. The flow and heat transfer physics are governed by four parameters: the rotational Reynolds number Re_ϕ, the buoyancy parameter $\beta\Delta T$, the compressibility parameter χ and the Rossby number Ro.

The model divides the cavity into two flow regions: lower radii driven by interaction with the throughflow and toroidal vortex; and higher radii driven by rotational buoyancy forces. It is assumed the boundary between the two regions occurs at the start of the disc diaphragm. The buoyancy effect in the outer region is induced by the disc rotation and the temperature difference between the shroud and throughflow. The heat is convected from the shroud via hot and cold radial plumes of fluid that travel inward and outward, respectively. The plume mass flow rate is determined using an empirical correlation established from unsteady pressure measurements. The effect of axial throughflow is twofold: it creates a toroidal vortex in the inner region and is directly ingested into the cold plumes in the outer region.

The model uses an exchange mass flow to account for the interaction between the flow in the cavity and the axial throughflow. The mass flow rate ψ_{ex} is related to the plume mass flow rate ψ_p. At low Ro, where the toroidal vortex is relatively weak, the ratio ψ_{ex}/ψ_p is maximised at the cavity width ratio, η. For a perfect open cavity (i.e. with uniform thickness), $\eta = 1$ and for the closed cavity $\eta = 0$. In addition, at low Ro, the flow in the axial region is subjected to flow reversal due to the extended circumferential pressure variation from anti- and cyclonic vortices. The model accounts for this effect by assuming the reversal flow comprises part of the exchange mass flow, increasing the average temperature of the exchange flow. At high Ro, where the toroidal vortex is enhanced, the ratio of ψ_{ex}/ψ_p reduces.

The convective shroud heat transfer is determined from free convection on horizontal plates, and the disc heat transfer is determined using conductive laminar Ekman layers. Radial and axial conduction through the disc is computed using an FEA solver. Correlations of the reversal flow and the exchange flow found in this paper are used to determine the core and plume temperatures. The model is solved iteratively until a heat balance is reached. Very good agreement has been achieved between the predicted and measured disc temperatures.

The effects of Re_ϕ, $\beta\Delta T$ and Ro on the disc temperature, θ_d, and the core temperature, θ_c, are discussed. θ_d is shown to be relatively insensitive to $\beta\Delta T$. Increasing Re_ϕ (and hence the compressibility parameter, χ) increases the radial increase in core temperature. Due to the impact of reversal and exchange mass flow, the impact of Ro is more complex. For $Ro < 0.4$, increasing Ro increases heat transfer in the cavity, lowering the cob temperatures and increasing the gradient of θ_d. At $Ro \sim 0.5$, there is an inflexion point (due to $\psi_r = 0$ and decreasing ψ_{ex}), whereby further increasing Ro increases θ_d at lower radii.

The model uncovers the nature of the mass and heat exchange between the flow in an open rotating cavity and the cold axial throughflow. It is anticipated that the model will be incorporated into engine design codes, informing the design of reliable and efficient gas turbine engines.

Acknowledgements

The research presented in this paper was supported by the UK Engineering and Physical Sciences Research Council and in collaboration with Rolls-Royce plc, under the grant number EP/P003702/1. The authors are very grateful for the support of Carl Sangan, Oliver Pountney and, especially, the late Professor J Michael Owen.

Nomenclature

Roman letters

A_1 = empirical reverse flow coefficient
A_2 = empirical exchange flow coefficient
a = inner radius of cavity (cob) [m]
a' = inner diaphragm radius [m]
b' = outer diaphragm radius [m]
b = outer radius of cavity (shroud) [m]
c_p = specific heat capacity [J/(kgK)]
d_H = hydrodynamic diameter of throughflow [m]
G = cavity gap ratio (= s/b)
h = heat transfer coefficient [W/(m^{2}K)]
k = thermal conductivity of air [W/(mK)]
k_d = thermal conductivity of disc [W/(mK)]
l = empirical exchange flow exponent

$\dot{m}$ = mass flow rate [kg/s]
n = number of vortex pairs
N = rotational speed of discs [RPM]
p = static pressure [Pa]
$\bar{p}$ = mean static pressure [Pa]
q = heat flux [W/m^2]
$\dot{Q}$ = heat flow [W]
r = radius [m]
R = specific gas constant (J/(kgK))
s = cavity width at diaphragm [m]
s' = cavity width at cobs [m]
t = thickness [m]
T = temperature [K]
W = throughflow velocity [m/s]
x = non-dimensional radial location
y = non-dimensional axial distance
z = axial distance [m]

Greek letters

α = angle between disc and radial direction [rad]
β = volume expansion coefficient [K^{-1}]
γ = ratio of specific heats
δ = Ekman layer thickness [m]
η = cavity width ratio (= s'/s)
θ = non-dimensional temperature (modelled)
Θ = non-dimensional temperature (measured)
μ = dynamic viscosity [kg/(ms)]
ρ = density [kg/m^3]
τ = non-dimensional heat flux
χ = compressibility parameter
ψ = non-dimensional mass flow rate
Ω = angular velocity [rad/s]

Dimensionless groups

$C_{\Delta p}$ = coefficient of pressure difference
Gr = Grashof number
Ma = rotational Mach number (= $\Omega b/\sqrt{\gamma R(T_a + T_b)}$)
Nu = Nusselt number
Pr = Prandtl number
Re = Reynolds number
Ro = Rossby number
$\beta\Delta T$ = buoyancy parameter (= $(T_{sh} + T_1)/T_1$)

Superscripts and subscripts

1 = value upstream in the axial throughflow
2 = value downstream in the axial throughflow
a = value at the inner radius of the cavity
a' = value at the inner radius of the diaphragm
b = value at the outer radius of the cavity
b' = value at the outer radius of the diaphragm
c = value in the fluid core
d = value on the disc surface
E = value in Ekman layers
ex = value in exchange mass flow
p = average value in radial plumes
$\check{p}, \hat{p}$ = values in the hot and cold plumes
r = value in reverse mass flow
f = value in the axial cooling flow
s = value of structures
sh = value on shroud surface
ϕ,r,z = circumferential, radial and axial direction

References

[1] Jackson, R. W., Tang, H., Scobie, J. A., Pountney, O. J., Sangan, C. M., Owen, J. M., and Lock, G. D., 2021, "Analysis of Shroud and Disk Heat Transfer in Aero-Engine Compressor Rotors," ASME. J. Eng. Gas Turbines Power, **143**(9), p. 091005.

[2] Owen, J. M. and Long, C. A., 2015, "Review of Buoyancy-Induced Flow in Rotating Cavities," ASME. J. Turbomach., **137**(11), p. 111001.

[3] Owen, J. M. and Pincombe, J. R., 1979, "Vortex Breakdown in a Rotating Cylindrical Cavity," J. Fluid Mech., **90**(1), pp. 109–127.

[4] Farthing, P. R., Long, C. A., Owen, J. M., and Pincombe, J. R., 1992, "Rotating Cavity With Axial Throughflow of Cooling Air: Flow Structure," ASME. J. Turbomach., **114**(1), pp. 237–246.

[5] Long, C. A., Miché, N. D. D., and Childs, P. R. N., 2007, "Flow measurements inside a heated multiple rotating cavity with axial throughflow," Int. J. Heat Fluid Flow, **28**(6), pp. 1391–1404.

[6] Fazeli, S. M., Kanjirakkad, V., and Long, C., 2021, "Experimental and Computational Investigation of Flow Structure in Buoyancy-Dominated Rotating Cavities," ASME. J. Eng. Gas Turbines Power, **7**(143), p. 071026.

[7] Black, J. and C.A., L., 1992, "Rotational coherent anti-stokes Raman spectroscopy measurements in a rotating cavity with axial throughflow of cooling air: oxygen concentration measurements." Appl. Opt., **31**(21), pp. 4291–4297.

[8] A., L. C., 1994, "Disk Heat Transfer in a Rotating Cavity with an Axial Throughflow of Cooling Air," Int. J. Heat and Fluid Flow, **15**(4), pp. 307–316.

[9] Günther, A., Uffrecht, W., and Odenbach, S., 2014, "The Effects of Rotation and Mass Flow on Local Heat Transfer in Rotating Cavities with Axial Throughflow," Proceedings of the ASME Turbo Expo 2014: Turbine Technical Conference and Exposition, **5C: Heat Transfer**, p. V05CT16A026.

[10] Jackson, R. W., Tang, H., Scobie, J. A., Pountney, O. J., Sangan, C. M., Owen, J. M., and Lock, G. D., 2022, "Unsteady Pressure Measurements in a Heated Rotating Cavity," Journal of Engineering for Gas Turbines and Power, **144**(4), p. 041017.

[11] Gao, F. and Chew, J. W., 2022, "Flow and Heat Transfer Mechanisms in a Rotating Compressor Cavity Under Centrifugal Buoyancy-Driven Convection," ASME. J. Eng. Gas Turbines Power, **144**(5), p. 051010.

[12] Pitz, D. B., Chew, J. W., and Marxen, O., 2019, "Effect of an axial throughflow on buoyancy-induced flow in a rotating cavity," Int. J. Heat Fluid Flow, **80**(12), p. 108468.

[13] Saini, D. and Sandberg, R. D., 2021, "Large-Eddy Simulations of High Rossby Number Flow in the High-Pressure Compressor Inter-Disk Cavity," ASME. J. Turbomach., **143**(11), p. 111002.

[14] Long, C. A. and Childs, P. R. N., 2007, "Shroud heat transfer measurements inside a heated multiple rotating cavity with axial throughflow," Int. J. Heat Fluid Flow, **28**(6), pp. 1405–1417.

[15] Owen, J. M. and Tang, H., 2015, "Theoretical Model of Buoyancy-Induced Flow in Rotating Cavities," ASME. J. Turbomach., **137**(11), p. 111005.

[16] Atkins, N. R. and Kanjirakkad, V., 2014, "Flow in a Rotating Cavity with Axial Throughflow at Engine Representative Conditions," Düsseldorf, Germany, June 16–20, p. V05CT16A041, doi: 10.1115/GT2014-27174.

[17] Tang, H., Puttock-Brown, M. R., and Owen, J. M., 2018, "Buoyancy-Induced Flow and Heat Transfer in Compressor Rotors," ASME. J. Eng. Gas Turbines Power, **140**(7), p. 071902.

[18] Jackson, R. W., Luberti, D., Tang, H., Pountney, O. J., Scobie, J. A., Sangan, C. M., Owen, J. M., and Lock, G. D., 2021, "Measurement and Analysis of Buoyancy-Induced Heat Transfer in Aero-Engine Compressor Rotors," ASME. J. Eng. Gas Turbines Power, **143**(6), p. 061004.

[19] Tang, H., Shardlow, T., and Owen, J. M., 2015, "Use of Fin Equation to Calculate Nusselt Numbers for Rotating Disks," ASME. J. Turbomach., **137**(12), p. 121003.

[20] Tang, H. and Owen, J., 2023, "Plume Model for Buoyancy-Induced Flow and Heat Transfer in Closed Rotating Cavities," ASME. J. Turbomach., **145**(1), p. 011005.

[21] Nicholas, T. E. W., Scobie, J. A., Lock, G. D., and Tang, H., 2023, "Transient Heat Transfer and Temperatures in Closed Compressor Rotors," Appl. Therm. Eng., submitted (2023).

[22] Lock, G. D., Jackson, R. W., Pernak, M., Pountney, O. J., Sangan, C. M., Owen, J. M., Tang, H., and Scobie, J. A., 2023, "Stratified and Buoyancy-Induced Flow in Closed Compressor Rotors," ASME. J. Turbomach., **145**(1), p. 011008.

[23] Pernak, M., Nicholas, T. E. W., Williams, J., Jackson, R. W., Tang, H., Lock, G. D., and Scobie, J. A., 2023, "Experimental Investigation of Transient Flow Phenomena in Rotating Compressor Cavities," Boston, USA, June 26-30, Paper No. GT2023-102294.

[24] Owen, J. M. and Rogers, R. H., 1988, *Flow and Heat Transfer in Rotating Disc Systems, Vol. 1: Rotor-stator systems*, Research Studies Press, Taunton, John Wiley, New York.

[25] Luberti, D., Patinios, M., Jackson, R. W., Tang, H., Pountney, O. J., Scobie, J. A., Sangan, C. M., Owen, J. M., and Lock, G. D., 2021, "Design and Testing of a Rig to Investigate Buoyancy-Induced Heat Transfer in Aero-Engine Compressor Rotors," ASME. J. Eng. Gas Turbines Power, **143**(4), p. 041030.